PAPER • OPEN ACCESS

Systematic extraction of a control-oriented model from perturbative experiments and SOLPS-ITER for emission front control in TCV

To cite this article: J.T.W. Koenders *et al* 2022 *Nucl. Fusion* **62** 066025

OPEN ACCESS
IOP Publishing | International Atomic Energy Agency Nuclear Fusion

Nucl. Fusion **62** (2022) 066025 (13pp) https://doi.org/10.1088/1741-4326/ac5b8c

Systematic extraction of a control-oriented model from perturbative experiments and SOLPS-ITER for emission front control in TCV

J.T.W. Koenders[1,2,*], M. Wensing[3], T. Ravensbergen[4], O. Février[3], A. Perek[1,3], M. van Berkel[1], the TCV Team[a] and the EUROfusion MST1 Team[b]

[1] DIFFER-Dutch Institute for Fundamental Energy Research, Eindhoven, Netherlands
[2] Department of Mechanical Engineering, Control Systems Technology Group, Eindhoven University of Technology, Eindhoven, Netherlands
[3] École Polytechnique Fédérale de Lausanne (EPFL), Swiss Plasma Center (SPC), Lausanne, Switzerland
[4] ITER Organization, St. Paul Lez Durance Cedex, France

E-mail: j.t.w.koenders@differ.nl

Received 17 January 2022, revised 3 March 2022
Accepted for publication 8 March 2022
Published 11 April 2022

Abstract

Systematic extraction of locally valid dynamic models from experiments is necessary for controller design and the validation of high fidelity models. This paper describes the extraction of a dynamic model in the form of a transfer function, giving the dynamic response of the CIII (465.0 nm) emission front position to deuterium gas puffing in the TCV divertor during flattop, relevant for heat exhaust control. The model is extracted using frequency response data from both SOLPS-ITER simulations and perturbative experiments. We use the steady-state solutions of the model SOLPS-ITER to obtain an additional data point at the zero frequency, as the identifiable frequency range by perturbative experiments is lower bounded by discharge time. We specifically approach the problem from a control engineering point of view, aiming to develop control-oriented models for the systematic design of impurity emission front controllers. We find a transfer function structure based on a diffusive process to best describe the obtained frequency response data. The resulting transfer function model accurately reproduces the local dynamic response measured during experiments, so it can be used to assess new controllers offline for similar discharge scenarios.

Keywords: power exhaust, system identification, detachment control, SOLPS-ITER

(Some figures may appear in colour only in the online journal)

* Author to whom any correspondence should be addressed.

[a] See Coda *et al* 2019 (https://doi.org/10.1088/1741-4326/ab25cb) for the TCV Team.
[b] See Labit *et al* 2019 (https://doi.org/10.1088/1741-4326/ab2211) for the EUROfusion MST1 Team.

1. Introduction

Reactor relevant tokamak operations require real-time control systems to reach and maintain advanced plasma scenarios [1]. The plasma state is analyzed using a large range of diagnostics, and steered in a desired direction using a multitude of actuators driven by real-time feedback control algorithms. These feedback control algorithms need to be designed systematically (using a model) to prevent excessive shot-to-shot controller tuning, and guarantee stability and performance. Development of control-oriented models is crucial for the systematic design of such feedback controllers [2]. Control-oriented models capture the dominant dynamic input–output behavior of a system with low complexity, and their inputs and outputs match the experimental case. The value of control-oriented models in fusion has proven its worth e.g., in suppressing tearing modes [3], control of sawtooth periods [4], density profile control [5, 6] and q-profile control [7]. In all of these works model-based controller design was applied, ranging from the relatively simple design method loop shaping [8], to advanced methods like model predictive control and robust control. Additionally, control-oriented models allow for the development of dynamic estimation techniques (e.g., Kalman filtering) to estimate and control unmeasured plasma parameters, necessary to overcome the sensor deprivation inherently present in fusion power plants.

In this paper, we synthesize a control-oriented model for a pressing problem: the real-time control of plasma detachment. Divertor plasma detachment is required to maintain a sufficient reduction of power flux densities impacting the divertor material [9]. Left unmitigated, the expected power fluxes during reactor relevant operation exceed present-day engineering limits [10, 11]. Detachment control is receiving large attention, with a range of control schemes being developed and demonstrated [12–16]. However, investigation of its dynamics (time-response) with respect to different actuators is largely overlooked. Notable exceptions include an investigation of the ITER divertor plasma response to impurities [17], emission front controller design using system identification [18] and power load feedback controller design based on first-principle modeling [19]. We specifically approach this problem from a control engineering point of view, aiming to develop control-oriented models for systematic detachment controller design.

We report on the systematic extraction of a first control-oriented model (in the form of a transfer function) of the divertor plasma response to deuterium gas puffing in tokamak à configuration variable (TCV) [20]. In TCV, the onset of detachment is correlated with CIII (465.0 nm) emission extinguishing near the divertor target [21–24]. This extinction near the target allows a CIII emission front position to be defined strongly related to the local electron temperature, typically 5–8 eV. We use this CIII emission front location to diagnose the dynamic response of the divertor plasma to deuterium gas puff. We combine perturbative dynamic identification experiments with SOLPS-ITER [25, 26] simulations to obtain frequency response function (FRF) data points, which are used to find a locally valid transfer function of the CIII front response to deuterium fueling. The governing dynamic process is unknown. Therefore, we consider three different transfer function structures which each depend on a different dynamic process: a time-delay, a first-order inventory model and a diffusion based model. From these, we find that the diffusion based model structure best describes the combination of perturbative measurements and SOLPS-ITER simulations. The extracted transfer function model is compared with experiments and found to accurately reproduce the experimentally observed dynamic response, which shows it can be used for offline design, and assessment of, feedback controllers which operate in a similar plasma scenario.

This paper is organized as follows: section 2 details the control problem, the use of perturbative experiments, and SOLPS-ITER, as a method to obtain FRF data. This section also includes explanations of control related notions as FRF's, transfer functions and Bode plots for the reader unfamiliar with this terminology. Section 3 describes the experimental set-up. Section 4, presents the perturbative experiments and SOLPS-ITER simulations and their resulting FRF data points. In section 5 we synthesize the three transfer function models, each with a different structure, and estimate their parameters with the obtained FRF data. The diffusion based model is found to best fit the FRF data, and is compared to additional experiments in section 6. We end with conclusions and a discussion in section 7.

2. Theoretical background

We introduce the general control loop in section 2.1, and the identification of the dynamics of a system which needs to be controlled in section 2.2. The reader familiar with general control theory and system identification can skip to section 2.3, where we detail the use of a time-independent model to complement perturbative identification experiments.

2.1. The control loop

Figure 1 shows the general control loop used as a basis for the majority of control theory [8, 27, 28]. To design a controller C with guarantees on stability and performance margins, the dynamics of the to be controlled plant H need to be identified. That is, how is the output y related to the input u of a dynamic system H. The plant H is often described by a differential equation. Most real systems have a non-linear input–output characteristic, however, a locally valid linear description is often sufficient to describe the dynamics within a certain operating range [27]. We denote such a locally valid description of the plant H as $\hat{H}$, which can be seen as a local linearisation of H around a certain operating point (y_0, u_0). Identifying $\hat{H}$ experimentally is done by exciting the system with carefully designed perturbations to the input u while measuring the output y. Under the assumption of small perturbations, a local linear approximation of H is identified which describes the relation of the output y to the input u at the operating point which was perturbed. The local linear approximation in the time domain takes the form of a linear time-invariant (LTI) ordinary differential equation (ODE). Such an ODE can be uniquely described by a FRF, which relates the relative amplitude

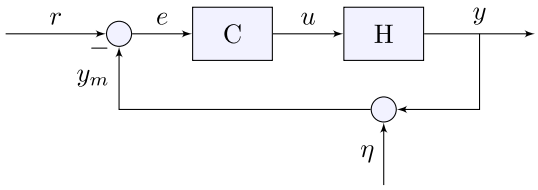

Figure 1. The general control loop. A desired reference r is compared with a measured output y_{m} subject to measurement noise η. The difference is the control error e which is fed to a controller C. The controller C computes the needed input u to steer the output y closer to its desired reference value r.

and phase of y with respect to u in the frequency domain. Therefore, a perturbation on u is generally done by using a periodic signal with specific frequency components [29]. We detail this with an example in the next section, where we translate an ODE to a transfer function and FRF and elaborate on how to identify it experimentally.

2.2. Experimental identification of the plant

Consider the local linearisation around (y_0, u_0) of the plant H: $\hat{H}$, to be a linear dynamic model as

$$\tau \frac{\mathrm{d}\delta y}{\mathrm{d}t}(t) = -\delta y(t) + k^* \delta u(t), \tag{1}$$

with input $\delta u = u(t) - u_0$, output $\delta y = y(t) - y_0$ and constants τ, k^*. Translation of (1) to the Laplace domain results in the transfer function $\hat{H}(s)$ as

$$\frac{\delta y(s)}{\delta u(s)} = \underbrace{\frac{k^*}{1+\tau s}}_{G(s)}, \tag{2}$$

with $s = \sigma + j\omega$ a complex number frequency parameter called the Laplace variable, with real numbers σ and ω. The FRF of (2) is obtained by evaluating its transfer function in the Fourier domain as $s = j\omega$, which can be interpreted as only looking at constant amplitude oscillations. We obtain a complex value for $\hat{H}(j\omega)$ per frequency ω (rad s^{-1}), which is the systems complex response per frequency, hence FRF. A system's FRF is depicted in a Bode diagram, showing the relative input–output magnitude and input–output phase per frequency. The magnitude is the absolute value of the complex response: $\left|\hat{H}(j\omega)\right|$, and the phase the angle between its real and imaginary part $\angle\hat{H}(j\omega)$. Identification of $\hat{H}(j\omega)$ can be done by injecting an input signal $\delta u(t)$ with specific frequency components and subsequently measuring the output $\delta y(t)$. Analyzing the relative phase and magnitude of $\delta y(t)$ with respect to $\delta u(t)$ over frequency then gives the system's FRF. FRF data points of $\hat{H}(j\omega)$ can then be used to estimate the parameters of a proposed transfer function $\hat{H}(s)$, in this case resulting in an estimate of the constants τ and k^*.

It is important to note that there is a strong additional benefit of the Laplace domain for analysis and design of linear systems and controllers. Namely, obtaining the output $y(t)$ of a linear system H for a given input $u(t)$ no longer requires the computation of the convolution

$$y(t) = H(t) * u(t) = \int_{\infty}^{\infty} H(\tau)u(t-\tau)\mathrm{d}\tau, \tag{3}$$

or solving the ODE. Instead the problem simplifies to a product

$$y(s) = H(s)u(s). \tag{4}$$

This means when considering the general control loop of figure 1, the closed-loop response of $r(s)$ to $y(s)$ becomes an analytic expression

$$y(s) = \frac{C(s)H(s)}{1 + C(s)H(s)} r(s). \tag{5}$$

Additionally, the plant $H(s)$ generally consists of an actuator $A(s)$, a process $G(s)$, and a sensor $S(s)$, with each a different transfer function. The plant is then a straightforward multiplication of those terms: $H(s) = S(s)G(s)A(s)$. Separately identified sensors and actuators can thus be analytically incorporated for analysis of the control-loop performance and stability.

2.3. Complementing perturbative experiments with a time-independent model

A FRF can be identified using perturbation experiments, of which the identifiable frequency range is limited by experimental time and hardware limits. For a meaningful computation of the variance and signal to noise ratio of FRF measurements, at least three periods of the lowest frequency in the chosen excitation signal is required [29]. Discharge duration is limited, which means the experimental time during which perturbations can be applied, τ_{exp} (s), is in the order of seconds for small to medium size tokamaks. This results in a lower bound on the identifiable frequency range of $3/\tau_{\mathrm{exp}}$ (Hz) considering the minimum of three periods. The upper limit of the identifiable frequency range is dictated by the limitation of the actuator (ability to inject signals at high frequency) and the sensor (ability to measure signals at high frequency). The resulting limited identifiable frequency range of an FRF can result in a non-unique identification of the parameters for a given transfer function. Figure 2 illustrates this, showing five different realizations (values for τ, k^*) of the transfer function $\hat{H}(s) = \frac{k^*}{1+\tau s}$ (2), which are indistinguishable when the identifiable frequency range by perturbative experiments is as depicted.

Although under weak assumptions FRF data around the desired closed-loop bandwidth is sufficient to design a controller with stability guarantees [8], uniquely identifying all transfer function parameters is desirable. Knowledge of all transfer function parameters means guarantees of both stability and performance of the closed-loop can be given for a given controller. In the case of figure 2 the measurement range limits the obtainable data to the already converged constant phase and constant amplitude slope. Additional data at lower frequencies than the characteristic pole location of $\hat{H}(s)$ (the frequency where the magnitude changes slope, and the phase crosses -45 degrees) is required to obtain a unique identification of τ, k^*. In section 4, we show the experimentally obtained FRF results from D_2

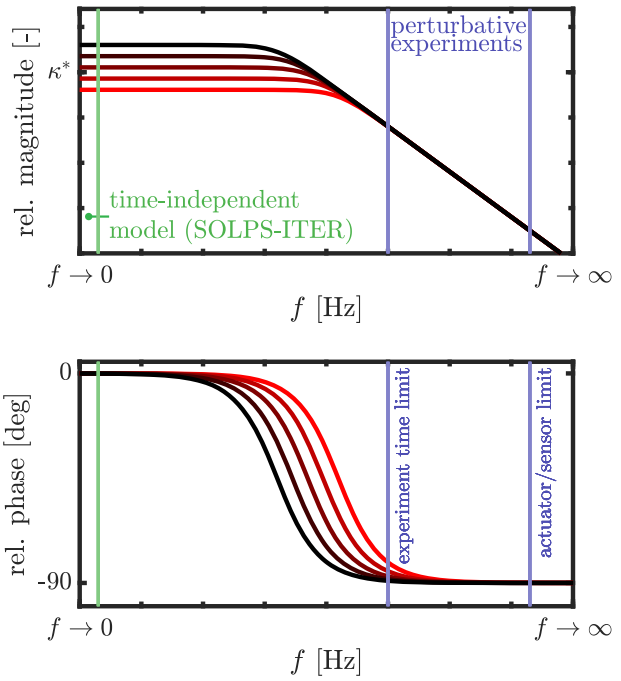

Figure 2. Bode diagram of a FRF. Five realizations of a transfer function model of the form $G(s) = \kappa^*/(1+\tau s)$. Top: the magnitude amplification per frequency, and bottom: the phase shift per frequency. The purple lines illustrate the experimental time and actuator/sensor limit of using perturbative experiments. A time-independent model (like steady-state SOLPS-ITER solutions) can identify an FRF data point at $f \to 0$, indicated in green.

gas puffing to CIII front position in TCV, are converged in phase and magnitude slope just like the example. Therefore, we complement the experiments by the use of a time-independent model, which can be used to obtain an additional FRF data point on the zero-frequency also called the DC-gain. We give here an explanation of this method by means of an example, the general derivation is detailed in appendix A.

Assume a time-independent model of the to be identified system is available. The time-independent model gives all equilibrium solutions $(y^{\mathrm{eq}}, u^{\mathrm{eq}})$, i.e. the points where $\frac{\mathrm{d}y}{\mathrm{d}t} = 0$. For the dynamic model (1) this yields

$$\frac{y^{\mathrm{eq}}}{u^{\mathrm{eq}}} = k^*. \tag{6}$$

This can be interpreted as the amplification of the converging output $y(t)|_{t\to\infty}$ with respect to some step input $\delta u(t) = c$, $\forall t \leqslant 0$, which is called the system's DC-gain. For stable systems, the final-value theorem states the DC-gain is equal to the transfer function evaluated at $s = 0$ [28]. A time-independent model of the system can thus be used to identify a specific point of the FRF: the one at the zero-frequency. In the case shown in figure 2 the DC-gain is equal to k^*. Combining the DC-gain gained from the time-independent model with the FRF data obtained by experiments now allows a unique identification of both k^* and τ. We take this exact approach to identify the parameters of a transfer function describing the dynamics from D_2 gas puffing to CIII front position in TCV: we combine FRF data from perturbative experiments with a DC-gain estimate obtained from steady-state SOLPS-ITER solutions.

Note that, it is possible to obtain the DC-gain experimentally. This requires a predefined input $u_{\mathrm{st}}(t)$ which brings the system to a stationary state y_1^{st}. A step input $\delta u(t) = c, \forall t \leqslant 0$, is then added to $u_{\mathrm{st}}(t)$ to reach a new stationary state y_2^{st}, leading to the DC-gain as $(y_2^{\mathrm{st}} - y_1^{\mathrm{st}})/c$. However, obtaining $u_{\mathrm{st}}(t)$ under time-varying conditions like wall-recycling, without using a controller is not trivial, making this a time-consuming option. This especially holds for machines where wall conditions do not saturate within a discharge, as is the case in TCV.

3. Experimental set-up

The experiments performed for this work were done on TCV [20]. Results are obtained using a lower single-null 250 kA Ohmic L-mode scenario in reversed field (unfavourable for H-mode access), with $\langle n_{\mathrm{e}} \rangle \approx 1 \times 10^{20}$ m^{-3} and $B_{\mathrm{tor}} = 1.4$ T.

3.1. Control goal

In TCV, the onset of detachment is correlated with CIII (465.0 nm) emission extinguishing near the divertor target [21–24], which allows an emission front to be defined. The location of this emission front is defined as a 50% emissivity decrease of CIII 465 nm emission along the divertor leg. The CIII front location is closely related to local electron temperature, typically 5–8 eV. Below this front, the electron temperatures reached in the divertor are sufficiently low for detachment enabling processes. It was shown that the CIII position can be controlled in real-time using fueling of D_2 by gas valve in the divertor [18]. We aim to identify a transfer function model $\hat{G}(s)$ which is capable of describing the local dynamic response from D_2 gas puff to CIII front location during flat top.

3.2. Sensor

The CIII emission front location is measured using a real-time detection algorithm [30] applied to spectrally filtered images originating from the multi-spectral imaging diagnostic MANTIS [31]. The MANTIS camera runs at 800 Hz and we use the time stamp of shutter opening plus half the exposure time ($\approx$0.5 ms) for each image. We define the output of our system y_{CIII} (m) as the distance of the CIII front from the target along the divertor leg.

3.3. Actuator

The front position can be controlled by the injection of D_2 molecules in the divertor using a piezo-electric gas valve [32]. The piezo-electric valve has a dynamic response from a requested gas flow to an actual gas flow, these dynamics have been identified separately and can be well described with an first-order plus dead time model. From the identification we obtained a valve bandwidth of 50 Hz, i.e. the valve cannot follow gas flow requests above 50 Hz. This induces the hardware limited upper bound on the identifiable frequency range at 50 Hz from our actuator. A pressure transducer in the valve is absolutely calibrated to measure the exact mass flow entering

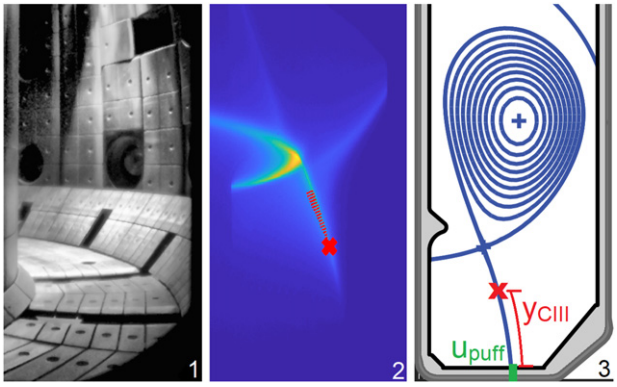

Figure 3. Overview of the control problem input and output. From left to right: (1) MANTIS view in the TCV vessel, (2) CIII 465 nm filtered image during one of the experiments with the identified CIII front location indicated with the red cross, (3) poloidal view of the equilibrium, definition of the front location (y_{CIII}) and valve location (u_{puff}). Equilibrium and MANTIS frame from discharge #63163.

the vacuum vessel, which we define as our input u_{puff} (D_2 s^{-1}). As we can measure the exact mass flow of D_2 entering the vessel as our input, the FRF data contains the plasma response only and not that of the valve itself.

Figure 3 shows an overview of the system with the MANTIS view, an example of the front identification algorithm, the definition of the front location (y_{CIII}), and the gas valve location (source of u_{puff}).

4. Results of perturbation experiments and SOLPS-ITER simulations

In this section we show the FRF results from perturbation experiments and the estimated DC-gain (FRF data point at the zero-frequency) from SOLPS-ITER simulations.

4.1. Measurement of the local frequency response with perturbative experiments

FRF data was obtained using sinusoidal perturbations around a feedforward of D_2 gas puff [18]. The used discharge scenario allows for a perturbation time τ_{exp} of approximately 1 s, placing a lower bound on the identifiable frequency range, or fundamental frequency f_0, at 3 Hz.

The perturbation applied to gas input is a multisine waveform, consisting of a sum of sinusoids with each a distinct frequency, phase and amplitude. Information on the specific design of the used multisine perturbations in these experiments can be found in [18], and more information on the general theory in [29, 33].

A perturbation was applied in two discharges: #63135 and #63163, where a multisine was injected with $f_0 = 6.25$ Hz with three harmonics and $f_0 = 4$ Hz with four harmonics, respectively. We define the gas-puff feedforward trajectory and corresponding unperturbed front trajectory as $u^{\mathrm{sol}}_{\mathrm{puff}}$ and $y^{\mathrm{sol}}_{\mathrm{CIII}}$, and the perturbation around this trajectory as δu_{puff} and δy_{CIII}. No back-to-back experiment without a perturbation has been performed, $y^{\mathrm{sol}}_{\mathrm{CIII}}$ is therefore estimated by a linear function through y_{CIII}. Figure 4 shows the input and output time traces

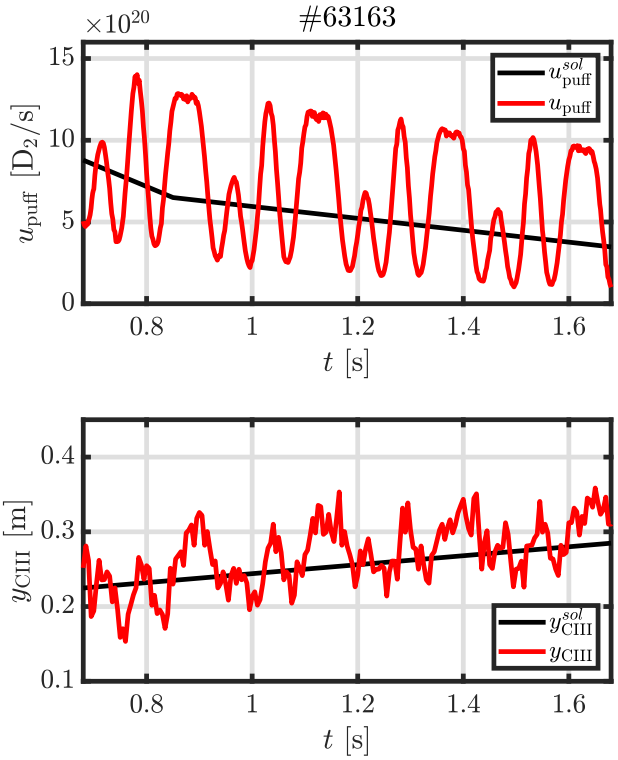

Figure 4. Time traces of system identification experiment #63163. Traces are shown for four periods of the 4 Hz fundamental frequency of the perturbation from 0.68–1.68 s. (top) Total deuterium gas-puff input u_{puff} and its feedforward trajectory $u^{\mathrm{sol}}_{\mathrm{puff}}$. (bottom) Total response of the CIII front location y_{CIII} and estimated trajectory due to feedforward only $y^{\mathrm{sol}}_{\mathrm{CIII}}$.

for discharge #63163 during the time window used for the perturbation analysis, exactly four periods of fundamental frequency $f_0 = 4$ Hz. As #63135 and #63163 are repeat discharges, we take the estimated $y^{\mathrm{sol}}_{\mathrm{CIII}}$ from #63163 to be equal for #63135.

Figure 5 shows the identified FRF data for the two experiments, including the 3 Hz lower bound and 50 Hz upper bound on the identifiable frequency range induced by τ_{exp} and the gas valve bandwidth respectively. The FRF data shows the phase to be roughly converged and no clear change of magnitude slope is present, indicating the need of FRF data below the measurement range to fit a (at least first order) transfer function. Therefore, as detailed in section 2.3, we estimate the DC-gain (response at the zero-frequency) of the system using SOLPS-ITER.

4.2. Estimation of the DC-gain using SOLPS-ITER

A scan of SOLPS-ITER [25, 26] simulations with different gas puff magnitudes based on the same magnetic equilibrium as the experiments (#62807, $t = 1$ s) are used to estimate the DC-gain. The simulations use a fixed heating power of 330 kW, comparable to the experiment, equally distributed between electrons and ions. The coupled Eirene code [25, 26] describes the neutral particle distribution using a kinetic Monte-Carlo approach. Atomic and molecular reactions as well as surface interactions are included. The simulations were performed both without and with full drifts, including both

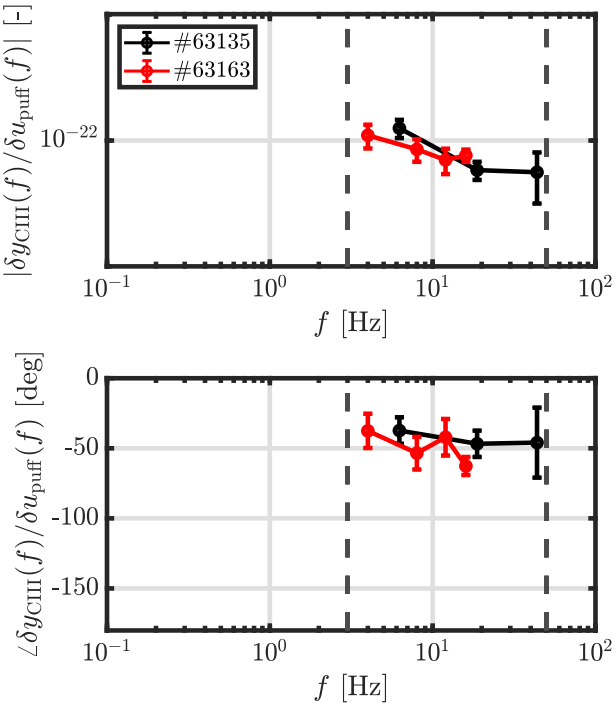

Figure 5. Frequency response measurements of the CIII emission front to multisine perturbations of deuterium gas-puff. Measurements are compensated for non-periodic behavior like transients using the local polynomial method as described in [33]. The 2σ errorbars are computed using the propagation of uncertainty for magnitude and phase as in [34], assuming a noiseless input case. The dashed lines indicate the lower and upper bound of the experimentally identifiable frequency range.

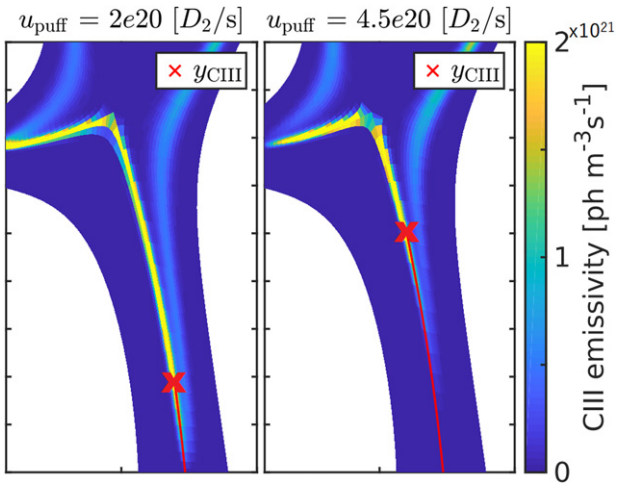

Figure 6. Identification of the CIII front location in SOLPS-ITER. The CIII front position is determined by taking the 50% emissivity decrease of CIII emissivity along the divertor leg. y_{CIII} is the distance from target to front along the seperatrix, indicated by the red line. A low fueling and high fueling case is shown with a relatively low and high front location respectively.

kinetic neutrals and carbon impurities [35]. During the scan of simulations the D_2 gas puff was increased from 0.5×10^{20} to $5 \times 10^{20} D_2$ s^{-1}. The gas input u_{puff} is introduced by a source at coordinates close to the experimental location.

For each simulation an analogous algorithm to [30] is used to identify the CIII front location, y_{CIII}. A region of interest is defined around the divertor leg consisting of a predefined number of cells to the left and right of the seperatrix, from the x-point to the target. For each cell the CIII (456.0 nm) emissivity is determined from the local plasma parameters using the ADAS database. The 50% emissivity decrease along the leg is then computed to pinpoint the CIII front location (as in the experiments), which is then translated to y_{CIII} by taking the poloidal distance along the seperatrix from the target to this point. From the simulations, an electron temperature of 7–10 eV at the CIII front position was identified [35]. Figure 6 shows the resulting identified front location for a relatively low- and high gas puff SOLPS-ITER simulation from the performed scan, these correspond to a low and high CIII front location respectively.

The CIII impurity emission front position, y_{CIII} is identified for each of the SOLPS-ITER simulations, resulting in a map of equilibrium solutions for the scan of constant gas source u_{puff}. We note here that the needed gas puff u_{puff} in SOLPS-ITER to reach a certain equilibrium is strongly dependent on the recycling coefficient c_{R}, and was observed to give similar results when $u_{\mathrm{puff}}(1 - c_{\mathrm{R}})$ is kept constant. For the used simulations, $c_{\mathrm{R}} = 99\%$ was chosen to closely reproduce the base discharge #62807 at $t = 1$ s. However, during experiments the recycling coefficient is not constant: the wall is slowly loaded with gas which leads to c_{R} approaching 100% over time. Therefore, we add an uncertainty of $\pm 15\%$ to the required gas puff u_{puff} to reach an equilibrium, which is the approximate change in gas puff to maintain a density flattop in the used scenario. The DC-gain is estimated by making a least squares fit using a 2nd order polynomial through the obtained equilibrium solutions, neglecting the data points for which $y_{\mathrm{CIII}} = 0$. Figure 7 shows the CIII front location for the equilibrium solutions obtained by the SOLPS-ITER simulations, data is shown for both the simulations with and without drifts. As the difference is minimal we make no distinction between these two cases and use both to estimate the DC-gain within the perturbation operating range.

The experimental perturbations were done around $y_{\mathrm{CIII}} \approx 0.24$ m, corresponding to the simulation input of $u_{\mathrm{puff}} \approx 4 \times 10^{20}$ (D_2 s^{-1}). We take the local derivative of the fitted polynomial at $u_{\mathrm{puff}} \approx 4 \times 10^{20}$ (D_2 s^{-1}) to obtain the local DC-gain of

$$\left.\frac{\delta y_{\mathrm{CIII}}(s)}{\delta u_{\mathrm{puff}}(s)}\right|_{s=0} = 4.22 \cdot 10^{-22}\ (\mathrm{m\,s^{-1}}). \tag{7}$$

In the next section, we propose three different transfer function models and estimate their parameters using the experimental FRF measurements and the obtained DC-gain from SOLPS-ITER.

5. Transfer function estimation

In this section, we take the experimental and simulation data obtained in section 4 and determine an appropriate transfer function model. There are several black-box methods to provide a good transfer function estimate of FRF data. The

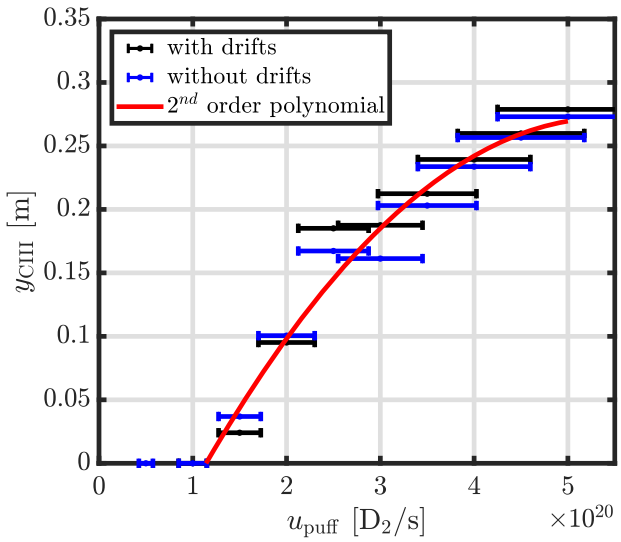

Figure 7. Obtained solutions of y_{CIII} for the scan of u_{puff} in SOLPS-ITER. The resulting fit yields $y_{\mathrm{CIII}} \cdot 10^{20} = -0.0149u_{\mathrm{puff}}^2 + 0.1611u_{\mathrm{puff}} - 0.1646$.

general approach is to find a minimum order transfer function polynomial of the form

$$\frac{y(s)}{u(s)} = \frac{b_0 s^m + b_1 s^{m-1} + \cdots + b_{m-1}s + b_m}{a_0 s^m + a_1 s^{m-1} + \cdots + a_{n-1}s + a_n}, \quad n \leqslant m, \quad (8)$$

which is able to describe the measurements [29]. However, this method does not yield any insight in the underlying mechanism of the measured process. Instead, we make an assumption on the process at play based on measurements and knowledge of the system, and derive a corresponding transfer function. The obtained FRF data is then used to estimate the parameters of this transfer function. The result gives insight in how well a suggested transfer function model can reproduce the obtained FRF data, and subsequently if the suggested process could be responsible for the measured dynamics. We take the ansatz that the neutral gas dynamics are the slowest time-scale of the chain of processes from gas injection to CIII front movement, and that the neutral gas dynamics are thus dominating our measurements. This coincides with earlier work in density control [36] and is supported by a clear proportionality between divertor neutral pressure and CIII front location during the perturbation experiments. Furthermore, preliminary results show the CIII front location is directly proportional to the total ionisation rate in the divertor, inferred from the Balmer series emissivity measured by MANTIS [37].

We derive three low order transfer functions with each a different approach of how these neutral dynamics can be described in a simple manner. These consist of: (1) a gain and delay model as used in [18], (2) a simplified extraction from the modeled gas injection dynamics in [5] as used in [36], and (3) a model based on diffusive neutral transport. These three models are based on the gas dynamics being dominated by: (1) convection, i.e. the neutrals travel a distance from the gas source to the plasma with constant (thermal) speed, (2) the ideal gas law, i.e. the vacuum volume outside the plasma being filled with neutrals, and (3) diffusion, i.e. neutral density buildup by a diffusive (collisional random walk) process from collisions within the plasma and the vessel wall. First the corresponding transfer function models are introduced, then we show the results of estimating their parameters with the data we obtained in section 4.

5.1. Gain and delay model

The transfer function model used for controller design of the same control problem (D_2 injection to CIII front location) in [18] was a 0th order gain and delay model as

$$\delta y_{\mathrm{CIII}}(t) = K\delta u_{\mathrm{puff}}(t - \tau_{\mathrm{delay}}), \quad (9)$$

with K the input–output gain and τ_{delay} the input–output delay. Transforming this model to the Laplace domain results in the transfer function

$$\delta y_{\mathrm{CIII}}(s) = \underbrace{Ke^{-s\tau_{\mathrm{delay}}}}_{\hat{G}_{\mathrm{del}}}\delta u_{\mathrm{puff}}. \quad (10)$$

The underlying mechanism can be interpreted as the injected gas needing to travel a certain distance d with constant (thermal) velocity v_{thermal} before interacting with the plasma. The parameter τ_{delay} should then be in the order of v_{thermal}/d, which for TCV results in ≈1 ms. The gain K describes the translation from the amount of injected neutrals to a change in CIII front position, here assumed constant over frequency. We term this transfer function model $\hat{G}_{\mathrm{del}}$.

5.2. Particle inventory model

As a second approach we use the most basic dynamic model contained in the particle inventory model approach of [5]. This model consists of three inventories, the plasma, the vacuum and the vessel wall. The plasma is modeled using a 1D profile, whereas the vacuum and wall inventories are modeled in 0D. A gas puff acts as the source of the system and a pump as the sink. The three inventories interact through a set of coupled differential equations, exchanging particles through e.g., ionization (vacuum to plasma), recombination (plasma to vacuum) and wall retention (plasma to wall). We consider here only the slowest time-scales of gas injection and (wall) pumping, and assume all other processes like ionization, recombination and plasma equilibration time are infinitely fast in comparison. This results in a simple 0D model for the neutral density as

$$\dot{n}_0(t) = -\frac{1}{\tau_{\mathrm{pump}}}n_0(t) + \frac{1}{V_0}u_{\mathrm{puff}}, \quad (11)$$

with n_0 (m^{-3}) the neutral density, a characteristic pump time τ_{pump} (s) and the vacuum volume V_0 (m^3), which is equal to the gas injection model used in [36]. We take a change in neutral density n_0 to be directly related to a change in front position y_{CIII} by an arbitrary unit scaling factor $\xi = 1 \times 10^{-22}$. Note that, this does not constrain the parameter estimation with the FRF data but simply allows V_0 and τ_{pump} to be in the

Table 1. Resulting parameters of transfer function fits.

Model	Parameter	Value	Unit
$\hat{G}_{\text{del}}$	K	1.191	—
	τ_{delay}	0.006	s
$\hat{G}_{\text{vol}}$	V_0	0.025	m^3
	τ_{pump}	0.107	s
$\hat{G}_{\text{diff}}$	D	0.025	$\text{m}^2\ \text{s}^{-1}$
	L	0.109	m

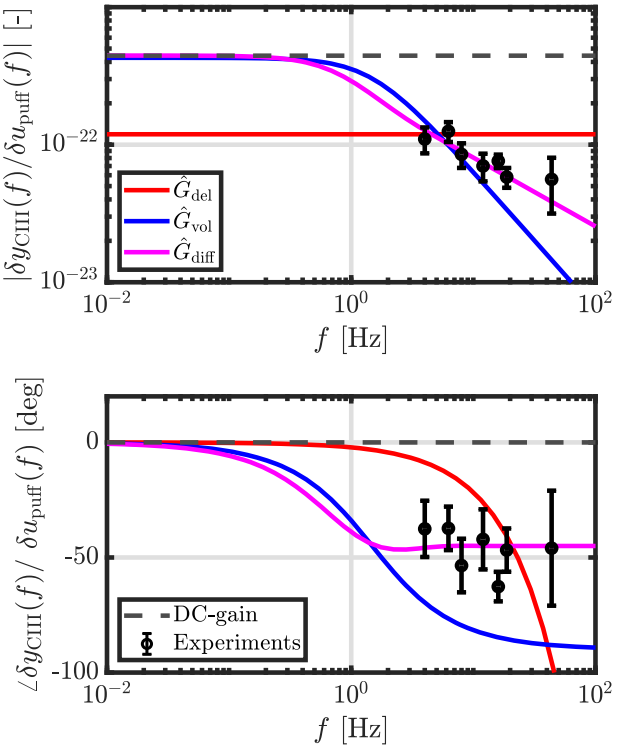

Figure 8. Results of the non-linear least squares fit of the transfer functions $\hat{G}_{\text{del}}$, $\hat{G}_{\text{vol}}$ and $\hat{G}_{\text{diff}}$ in the frequency domain. Only for $\hat{G}_{\text{diff}}$ a fit is obtained which is able to describe both the FRF measurements and the obtained DC-gain from SOLPS-ITER.

correct order of magnitude. The resulting transfer function for the local dynamics is then

$$\delta y_{\text{CIII}}(s) = \underbrace{\xi \frac{1/V_0}{s + 1/\tau_{\text{pump}}}}_{\hat{G}_{\text{vol}}} \delta u_{\text{puff}}(s), \tag{12}$$

we term this transfer function model $\hat{G}_{\text{vol}}$.

5.3. Diffusion based model

The measured phase behavior and magnitude slope as shown in figure 5 approximately converge to a phase of $\approx -50^{\circ}$ with a magnitude slope of ≈ -12 dB per decade frequency. This behavior is reminiscent of the Warburg-domain, which can indicate a diffusive mechanism is at play [38]. In the Warburg-domain a transfer function is described in polynomials of the $\sqrt{s}$ instead of s as in the Laplace domain. Based on the observation of Warburg-domain like phase and magnitude behavior, we consider the possibility of a (quasi) diffusive process

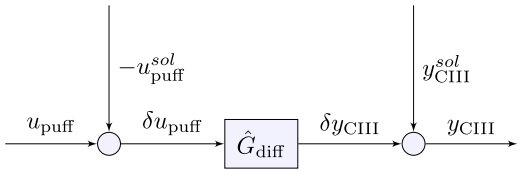

Figure 9. Framework of the verification. The signals are the total injected D_2 u_{puff}, programmed feedforward $u^{\text{sol}}_{\text{puff}}$, perturbed input δu_{puff}, perturbed output δy_{CIII}, unperturbed output $y^{\text{sol}}_{\text{CIII}}$ and total output y_{CIII}.

dominating the gas dynamics from D_2 injection to neutral density buildup. We define a spatial domain x, with $x = 0$ the valve source at the divertor target and $x = L$ the end of the domain where all neutrals are ionised. The model structure then becomes

$$\frac{\partial n_0(x,t)}{\partial t} = D \frac{\partial^2 n_0(x,t)}{\partial x^2}, \tag{13}$$

with boundary conditions

$$\begin{aligned} -D \frac{\partial n_0(x,t)}{\partial x}|_{x=0} &= \delta u_{\text{puff}}(t), \\ n_0(x,t)|_{x=L} &= 0, \end{aligned} \tag{14}$$

with D ($\text{m}^2\ \text{s}^{-1}$) the diffusion coefficient and $n_0(x,t)$ (m^{-3}) the neutral density. Transforming the problem to the Laplace domain and using the general solution [39] results in the transfer function

$$n_0(x,s) = \frac{\cosh(x\lambda)\tanh(L\lambda) - \sinh(x\lambda)}{D\lambda} \delta u_{\text{puff}}(s), \tag{15}$$

with $\lambda = \sqrt{s/D}$, showing the dependence on $\sqrt{s}$. As previously, we assume a change in target neutral density $\delta n_0(0,s)$ is directly related to a change in front position δy_{CIII} by a unit scaling factor $\xi = 1 \times 10^{-22}$. The final model structure then becomes

$$\delta y_{\text{CIII}}(s) = \underbrace{\xi \frac{\tanh(L\lambda)}{D\lambda}}_{\hat{G}_{\text{diff}}} \delta u_{\text{puff}}(s), \tag{16}$$

we term this transfer function model $\hat{G}_{\text{diff}}$.

5.4. Estimation results

We estimate the parameters of each transfer function model by fitting their response on the obtained FRF data in the complex plane using a non-linear least squares optimization. We use both measured FRF data and the DC-gain estimate from the SOLPS-ITER simulations, the DC-gain estimate is positioned at 10^{-5} Hz for numerical reasons. As all errorbars are in the same order of magnitude, no additional uncertainty weighting is implemented. Table 1 and figure 8 show the resulting estimated model parameters.

The estimated gain and delay model $\hat{G}_{\text{del}}$ is unable to describe the FRF measurements as this model assumes no decay of relative amplitude over frequency. Furthermore, the phase drops linearly with frequency, which is also not observed in the measurements.

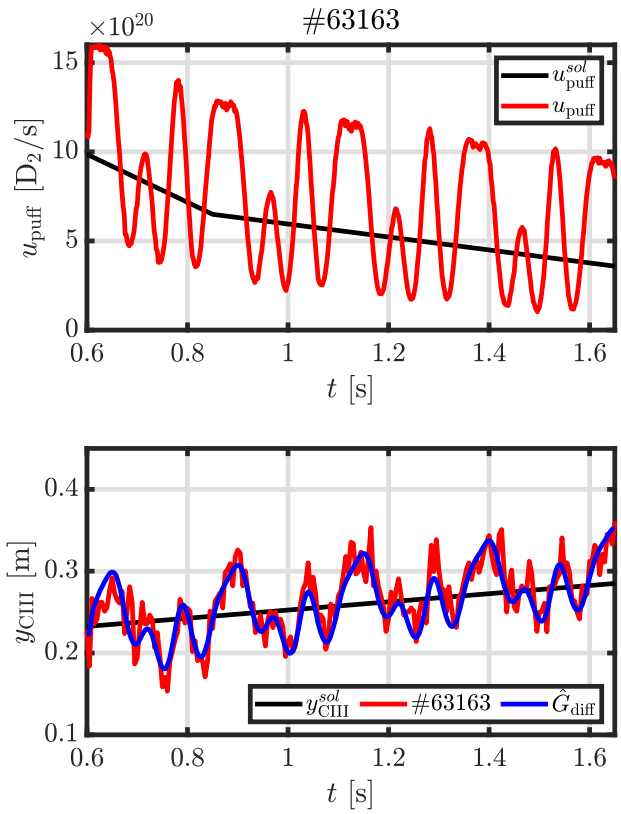

Figure 10. Open-loop verification with a perturbation experiment. Top: feedforward input $u^{\mathrm{sol}}_{\mathrm{puff}}$ and total input u_{puff} used as an input for the model (see figure 9). Bottom: unperturbed output $y^{\mathrm{sol}}_{\mathrm{CIII}}$, and experimental and modeled CIII front location.

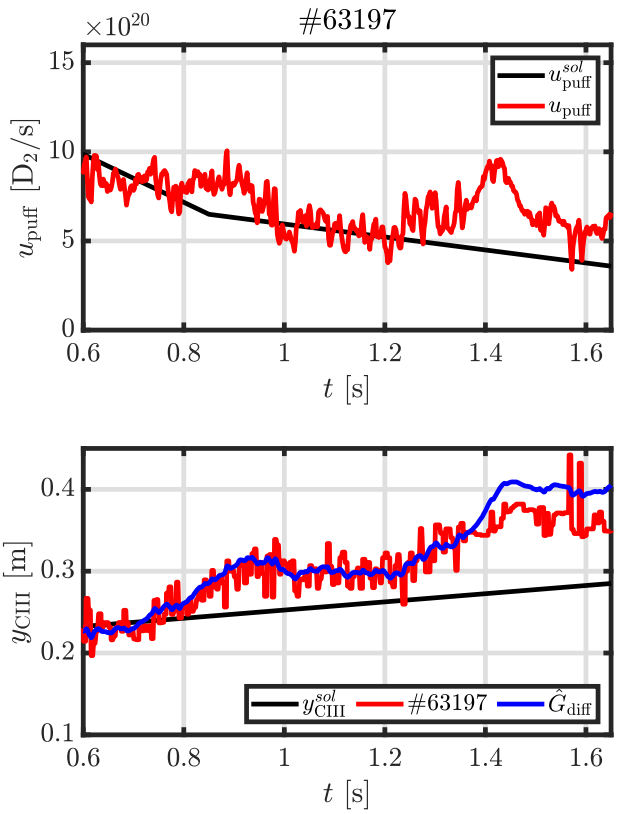

Figure 11. Open-loop verification with a controlled gas puff experiment. Signals as in figure 10.

The first-order model $\hat{G}_{\mathrm{vol}}$ comes closer to the FRF data and can also describe a change in magnitude from DC-gain in lower frequencies to a decay of relative amplitude with frequency. However, this models phase converges to $-90°$ whereas the measured phase is closer to a converged $-45°$. Furthermore, the decay over frequency of the relative amplitude is significantly stronger than measured.

We find the diffusion based model $\hat{G}_{\mathrm{diff}}$ is able to correctly describe both the FRF measurements and DC-gain estimate from SOLPS-ITER simulations. Therefore, we verify the model $\hat{G}_{\mathrm{diff}}$ with additional experimental data in the next section.

6. Verification of the diffusion based transfer function with experiments in the time domain

In this section, we verify the obtained local transfer function model $\hat{G}_{\mathrm{diff}}$ with experimental data in the time domain. We use the perturbation discharge #63163, and the repeat discharge #63197 where the front was moved upwards by a controlled density puff. Both have equal programmed feedforward traces $u^{\mathrm{sol}}_{\mathrm{puff}}$. We again assume the estimated unperturbed trajectory of the CIII front position from the feedforward $y^{\mathrm{sol}}_{\mathrm{CIII}}$ as shown in figure 4, is equal for both. Note $\hat{G}_{\mathrm{diff}}$ is a non-rational transfer function and therefore not trivially simulated in the time domain. We use the Chebyshev collocation method [39] to obtain a time-domain description of $\hat{G}_{\mathrm{diff}}$, which is essentially a state-space approximation of the transfer function using Chebyshev polynomials. An approximation of order 20 was found to be adequate for the frequency range relevant to this work. An exact time-domain representation of $\hat{G}_{\mathrm{diff}}$ using an infinite-sum representation as in [40] can be found in appendix B. The comparison with a perturbation experiment and a controlled puff experiment can be seen as a relatively high and low frequency verification of the transfer function model respectively. Figure 9 shows the framework of the verification.

From the experiments, we take the programmed feedforward $u^{\mathrm{sol}}_{\mathrm{puff}}$, the total gas injection u_{puff}, and the estimated unperturbed output trajectory $y^{\mathrm{sol}}_{\mathrm{CIII}}$ as shown in figure 4. We compare the time-traces from $t = 0.6$ s to $t = 1.68$ s which corresponds to the start of the density flat-top and the start of plasma current ramp down respectively. The model is initialized with the experimental value of the front position y_{CIII} and total input u_{puff} at $t = 0.6$ s. Note that, it is possible that $\delta u_{\mathrm{puff}} > 0$ at the start of the simulation, as a density controller is active up until this point. Figures 10 and 11 show the experimental results and their corresponding simulation output. In both cases good agreement is obtained between the model and experiments indicating its local validity around the feedforward trajectory. In figure 11 a deviation is observed after $t = 1.4$ s, which can indicate that at this point the CIII front is located outside the locally valid operating range of the model. This is in line with the results from the SOLPS-ITER simulations from figure 7, which shows the effect of an increased gas puff is decaying for a higher CIII front position. The model $\hat{G}_{\mathrm{diff}}$ is able

to accurately reproduce experiments in both high- and low-frequency ranges around the feedforward trajectory, which validates the model for controller design for bandwidths within the measured frequency range.

7. Conclusions and discussion

Systematic design of controllers requires a control-oriented model of the input–output dynamics of the system. A control-oriented model should capture the dynamic behavior of a system with low complexity, in a desired operating range. In this paper, we have shown a systematic approach to obtain a transfer function model when FRF measurements are limited in frequency range. The model describes the response of the CIII impurity emission front position to D_2 gas puff in the divertor of TCV. FRF data points were obtained from periodic perturbation experiments. An additional data point at the zero frequency was estimated using the steady-state solutions of the model SOLPS-ITER, to gather information outside the measurable frequency range. Based on previous work, we assumed the neutral gas injection dynamics are dominating the measured response, and therefore fitted three different transfer functions based on different mechanisms describing these neutral dynamics. A diffusion based transfer function was shown to best describe the combination of perturbative measurements and estimated DC-gain using SOLPS-ITER, which points toward a (quasi) diffusive process being at play. The obtained transfer functions dynamic response was verified with experiments where it was shown the model is able to accurately reproduce the experimentally obtained response of the CIII impurity emission front to D_2 gas puff in the divertor. From this we conclude the model is fit to use for offline controller design, and can be used to design for specific control requirements for repeat discharges.

Note that, strictly speaking, guarantees for the obtained transfer function model can only be given locally, which means it is only valid during the (density) flattop of a single scenario and its repeats. Depending on the nonlinearity of the underlying dynamics, the operational range where the model is valid might be extended.

Additionally, a diffusive-based model fitting the FRF data does not prove a diffusive mechanism is at play, but does provide a clear direction for the further investigation of control-oriented dynamic gas injection models in tokamaks. Possibly the multiple reflections of neutrals at vessel walls and plasma boundary before ionisation act as a quasi diffusive process.

Finally, we have shown a single identification experiment in combination with an available time-independent model is enough to obtain a transfer function model useable for offline controller design, and useful for e.g., pulse design simulator tools like Fenix [41]. Obtaining dynamic models experimentally, and trying to obtain a physical understanding of the processes dominating perturbative measurements, can give insight in what processes need to be modeled with explicit time dependence in control-oriented models. Physics based dynamic models can then be validated with experimental data obtained from these perturbative experiments. For example, by applying system identification methods on time-dependent SOLPS-ITER simulations, and comparing the results with experiments. The systematic approach presented in this paper hopefully supports the further development of such dynamic models for relevant control problems in tokamaks like detachment control.

Acknowledgments

The authors thank Dr H. Reimerdes and Prof. H.J. Zwart for their valuable input on the manuscript. Experimental support of the TCV team is greatly appreciated. This work was supported in part by the Swiss National Science Foundation. This work has been carried out within the framework of the EUROfusion Consortium, funded by the European Union via the Euratom Research and Training Programme (Grant Agreement No. 101052200—EUROfusion). Views and opinions expressed are however those of the author(s) only and do not necessarily reflect those of the European Union or the European Commission. Neither the European Union nor the European Commission can be held responsible for them.

Appendix A. Theoretical background: the system theory representation

For this work, we consider the general class of physical systems defined by nonlinear differential equations of the form [27]

$$\begin{aligned} \dot{x} &= f(x,u), \\ y &= g(x,u), \end{aligned} \tag{A.1}$$

with state variable $x \in \mathcal{R}^n$, input variable $u \in \mathcal{R}^k$ and output variable $y \in \mathcal{R}^m$. We define (A.1) as the *global* dynamics of the system. A locally valid linear model can be identified by applying small perturbations around a solution to (A.1). Let us consider an arbitrary solution

$$\begin{aligned} u^{\mathrm{sol}} &: [0\ \infty) \to \mathcal{R}^k, \\ x^{\mathrm{sol}} &: [0\ \infty) \to \mathcal{R}^n, \\ y^{\mathrm{sol}} &: [0\ \infty) \to \mathcal{R}^m, \end{aligned} \tag{A.2}$$

which is not necessarily constant in time, i.e., it can either be a trajectory or an equilibrium point. Applying an input

$$u(t) = u^{\mathrm{sol}}(t) + \delta u(t), \quad \forall t \geqslant 0, \tag{A.3}$$

will lead to a corresponding output $y(t)$ which is perturbed with respect to $y^{\mathrm{sol}}(t)$. The perturbation of $x(t)$ and $y(t)$ can then be investigated by defining

$$\begin{aligned} \delta x(t) &:= x(t) - x^{\mathrm{sol}}(t), \\ \delta y(t) &:= y(t) - y^{\mathrm{sol}}(t). \end{aligned} \tag{A.4}$$

The dynamics of the perturbation are then obtained by taking the Taylor series expansion around the solution as

$$\begin{aligned}\delta\dot{x} &= \frac{\partial f(x^{\mathrm{sol}}(t),u^{\mathrm{sol}}(t))}{\partial x}\delta x + \frac{\partial f(x^{\mathrm{sol}}(t),u^{\mathrm{sol}}(t))}{\partial u}\delta u \\ &\quad + \mathcal{O}(\|\delta x\|^2) + \mathcal{O}(\|\delta u\|^2), \\ \delta y &= \frac{\partial g(x^{\mathrm{sol}}(t),u^{\mathrm{sol}}(t))}{\partial x}\delta x + \frac{\partial g(x^{\mathrm{sol}}(t),u^{\mathrm{sol}}(t))}{\partial u}\delta u \\ &\quad + \mathcal{O}(\|\delta x\|^2) + \mathcal{O}(\|\delta u\|^2).\end{aligned} \tag{A.5}$$

Under the assumption of sufficiently small perturbations, we only need to retain the first-order terms [42]. This results in the linearised *local* dynamics, where local means around a trajectory or equilibrium point. This local linear model can be represented as a linear state-space system

$$\begin{aligned}\delta\dot{\hat{x}} &= A(t)\delta\hat{x} + B(t)\delta u, \\ \delta\hat{y} &= C(t)\delta\hat{x} + D(t)\delta u,\end{aligned} \tag{A.6}$$

with Jacobian matrices

$$\begin{aligned}A(t) &:= \frac{\partial f(x^{\mathrm{sol}}(t),u^{\mathrm{sol}}(t))}{\partial x}, \\ B(t) &:= \frac{\partial f(x^{\mathrm{sol}}(t),u^{\mathrm{sol}}(t))}{\partial u}, \\ C(t) &:= \frac{\partial g(x^{\mathrm{sol}}(t),u^{\mathrm{sol}}(t))}{\partial x}, \\ D(t) &:= \frac{\partial g(x^{\mathrm{sol}}(t),u^{\mathrm{sol}}(t))}{\partial u}.\end{aligned} \tag{A.7}$$

Finally, we assume the solution $(x^{\mathrm{sol}}, u^{\mathrm{sol}})$ to be sufficiently bounded to neglect the time dependence of the matrices A, B, C and D. This inherently means we assume the local dynamics can be described by a LTI system for the whole considered trajectory $(x^{\mathrm{sol}}, u^{\mathrm{sol}})$. Input–output dynamics of LTI systems can be uniquely described by a transfer function in the Laplace domain as $\mathcal{L}(\delta\hat{y}(t))/\mathcal{L}(\delta u(t))$. We can transform (A.6) under the assumption of its time-invariance to the transfer function $G(s)$ as

$$\delta\hat{y}(s) = \underbrace{\left(C(sI-A)^{-1}B + D\right)}_{G(s)}\,\delta u(s). \tag{A.8}$$

Let a time-independent model of the global dynamics be available, which essentially gives all equilibrium solutions $(y^{\mathrm{sol}}, u^{\mathrm{sol}})$ to (A.1), i.e. $\dot{x} = 0$. For stable systems, the time-independent model gives the converging output over a step-input

$$\left.\frac{\delta y(t)}{\delta u(t)}\right|_{t\to\infty} = \left.\frac{y(t) - y^{\mathrm{sol}}}{u(t) - u^{\mathrm{sol}}}\right|_{t\to\infty}, \tag{A.9}$$

for some step input $\delta u(t) = c, \forall t \leqslant 0$. The local DC-gain can then be obtained by taking the local derivative of the equilibrium solutions $\partial y^{\mathrm{eq}}/\partial u^{\mathrm{eq}}$ around a chosen equilibrium point or trajectory $(y^{\mathrm{sol}}, u^{\mathrm{sol}})$. For stable systems, the final-value theorem states the DC-gain is equal to the transfer function evaluated at $s = 0$ [28]. Under the assumption of stable systems, the obtained local DC-gain is then the relative input–output magnitude on the zero-frequency, where the phase is necessarily zero. From this, we conclude a time-independent model of the global dynamics can be used to identify a point of the FRF of the local linearised dynamics at the zero-frequency, reducing the problem of a limited FRF measurement range, and solving it in the case of figure 2.

Appendix B. Time-domain representation of the diffusion based transfer function

The transfer function model $\hat{G}_{\mathrm{diff}}(s)$ (16) is of a distributed parameter system, or *boundary control problem*, and therefore an irrational function. Contrary to rational transfer functions, $\hat{G}_{\mathrm{diff}}(s)$ has an infinite number of poles and zeros, and can be represented by an infinite sum of rational transfer functions. Its time-domain representation is then simply the inverse Laplace-transform of the infinite sum representation of rational functions in s. We derive here the time-domain representation of $\hat{G}_{\mathrm{diff}}$, and refer to [40, 43] for more details on distributed parameter systems. First, we rewrite $\hat{G}_{\mathrm{diff}}$ to

$$\hat{G}_{\mathrm{diff}}(s) = \frac{\xi}{D}\frac{\sinh(L\lambda)}{\lambda\cosh(L\lambda)}, \tag{B.1}$$

with ξ, D, L and λ as in section 5.3. The poles of (B.1) are obtained from setting the denominator to 0 from which we obtain

$$\begin{aligned}L\lambda &= (\pi/2 + k\pi)i, \\ L^2\lambda^2 &= -(\pi/2 + k\pi)^2.\end{aligned} \tag{B.2}$$

Substituting $\lambda = \sqrt{\frac{s}{D}}$ leads to the systems pole locations at

$$p_k = -(\pi/2 + k\pi)^2\frac{D}{L^2}, \quad \text{for } k = 0, 1, 2\ldots. \tag{B.3}$$

Note that, from first view (B.1) seems to have pole at $s = 0$. However, it can be shown that $\lim_{s\to 0}\hat{G}_{\mathrm{diff}}(s) = \frac{\xi L}{D}$ and therefore $s = 0$ is not a pole of (B.1). The obtained poles p_k will be used for the denominator of the infinite sum representation. The numerator z_k of the infinite sum representation is found by computing

$$z_k = \lim_{s\to p_k}(s - p_k)\hat{G}_{\mathrm{diff}}(s). \tag{B.4}$$

which, after some algebra, reduces to $z_k = \frac{2\xi}{L}$. The infinite sum representation of (B.1) becomes

$$\hat{G}_{\mathrm{diff}}(s) = \sum_{k=0}^{\infty}\frac{z_k}{s - p_k} = \sum_{k=0}^{\infty}\frac{\frac{2\xi}{L}}{s + (\pi/2 + k\pi)^2\frac{D}{L^2}}. \tag{B.5}$$

We can now apply the inverse Laplace transform to obtain

$$\hat{H}_{\mathrm{diff}}(t) = \sum_{k=0}^{\infty}\frac{2\xi}{L}\exp\left[-(\pi/2 + k\pi)^2\frac{D}{L^2}t\right], \tag{B.6}$$

as the time-domain representation of $\hat{G}_{\mathrm{diff}}(s)$. Note that, $\hat{H}_{\mathrm{diff}}(t)$ is only defined for $t > 0$.

ORCID iDs

J.T.W. Koenders https://orcid.org/0000-0003-4385-923X
M. Wensing https://orcid.org/0000-0003-4462-7860
T. Ravensbergen https://orcid.org/0000-0001-7347-5515
O. Février https://orcid.org/0000-0002-9290-7413
A. Perek https://orcid.org/0000-0002-4117-0298
M. van Berkel https://orcid.org/0000-0001-6574-3823

References

[1] Humphreys D. *et al* 2015 Novel aspects of plasma control in ITER *Phys. Plasmas* **22** 021806
[2] Franklin G.F. *et al* 2019 *Feedback Control of Dynamical Systems* 8th edn (New York: Pearson)
[3] Hennen B.A., Westerhof E., Nuij P.W.J.M., de Baar M.R. and Steinbuch M. 2012 Systematic design and simulation of a tearing mode suppression feedback control system for the TEXTOR tokamak *Nucl. Fusion* **52** 074009
[4] Witvoet G., de Baar M.R., Westerhof E., Steinbuch M. and Doelman N.J. 2011 Systematic design of a sawtooth period feedback controller using a Kadomtsev–Porcelli sawtooth model *Nucl. Fusion* **51** 073024
[5] Blanken T.C., Felici F., Rapson C.J., de Baar M.R. and Heemels W.P.M.H. 2018 Control-oriented modeling of the plasma particle density in tokamaks and application to real-time density profile reconstruction *Fusion Eng. Des.* **126** 87–103
[6] Bosman T.O.S.J., Kudláček O., Fable E., van Berkel M., Felici F., Bock A., Luda T. and de Baar M.R. 2021 Kalman filter density reconstruction in ICRH discharges on ASDEX Upgrade *Fusion Eng. Des.* **170** 112510
[7] Felici F., Citrin J., Teplukhina A.A., Redondo J., Bourdelle C., Imbeaux F. and Sauter O. 2018 Real-time-capable prediction of temperature and density profiles in a tokamak using RAPTOR and a first-principle-based transport model *Nucl. Fusion* **58** 096006
[8] Skogestad S. and Postlethwaite I. 2007 *Multivariable Feedback Control: Analysis and Design* 2nd edn (New York: Wiley)
[9] Lipschultz B. *et al* 2016 Sensitivity of detachment extent to magnetic configuration and external parameters *Nucl. Fusion* **56** 056007
[10] Loarte A. *et al* 2007 Progress in the ITER physics basis chapter 4: power and particle control *Nucl. Fusion* **47** 203
[11] Pitts R.A. *et al* 2019 Physics basis for the first ITER tungsten divertor *Nucl. Mater. Energy* **20** 100696
[12] Khodunov I. *et al* 2021 Real-time feedback system for divertor heat flux control at COMPASS tokamak *Plasma Phys. Control. Fusion* **63** 065012
[13] Eldon D. *et al* 2019 Advances in radiated power control at DIII-D *Nucl. Mater. Energy* **18** 285–90
[14] Wu K., Yuan Q.P., Xiao B.J., Chen J.B., Duan Y.M., Zheng X.W., Wang L., Luo Z.P. and Liu X.J. 2018 Radiative feedback control on EAST *Fusion Eng. Des.* **129** 291–3
[15] Xu G.S. *et al* 2020 Divertor impurity seeding with a new feedback control scheme for maintaining good core confinement in grassy-ELM H-mode regime with tungsten monoblock divertor in EAST *Nucl. Fusion* **60** 086001
[16] Bernert M. *et al* 2021 *X*-point radiation, its control and an ELM suppressed radiating regime at the ASDEX Upgrade tokamak *Nucl. Fusion* **61** 024001
[17] Bonnin X., Pitts R.A., Komarov V., Escourbiac F., Merola M., Bo L., Wei L., Pan L. and Kukushkin A.S. 2017 ITER divertor plasma response to time-dependent impurity injection *Nucl. Mater. Energy* **12** 1100–5
[18] Ravensbergen T. *et al* 2021 Real-time feedback control of the impurity emission front in tokamak divertor plasmas *Nat. Commun.* **12** 1105
[19] Kallenbach A. *et al* 2010 Divertor power load feedback with nitrogen seeding in ASDEX Upgrade *Plasma Phys. Control. Fusion* **52** 055002
[20] Coda S. *et al* 2019 Physics research on the TCV tokamak facility: from conventional to alternative scenarios and beyond *Nucl. Fusion* **59** 112023
[21] Theiler C. *et al* 2017 Results from recent detachment experiments in alternative divertor configurations on TCV *Nucl. Fusion* **57** 072008
[22] Harrison J.R. *et al* 2017 Detachment evolution on the TCV tokamak *Nucl. Mater. Energy* **12** 1071–6
[23] Harrison J.R. *et al* 2019 Progress toward divertor detachment on TCV within H-mode operating parameters *Plasma Phys. Control. Fusion* **61** 065024
[24] Février O. *et al* 2020 Nitrogen-seeded divertor detachment in TCV L-mode plasmas *Plasma Phys. Control. Fusion* **62** 035017
[25] Wiesen S. *et al* 2015 The new SOLPS-ITER code package *J. Nucl. Mater.* **463** 480–4
[26] Bonnin X., Dekeyser W., Pitts R., Coster D., Voskoboynikov S. and Wiesen S. 2016 Presentation of the new SOLPS-ITER code package for tokamak plasma edge modelling *Plasma Fusion Res.* **11** 1403102
[27] Hespanha J. 2009 *Linear Systems Theory* (Princeton, NJ: Princeton University Press)
[28] Ogata K. 2002 *Modern Control Engineering* 4th edn (Englewood Cliffs, NJ: Prentice-Hall)
[29] Pintelon R. and Schoukens J. 2012 *System Identification: A Frequency Domain Approach* 2nd edn (New York: Wiley)
[30] Ravensbergen T. *et al* 2020 Development of a real-time algorithm for detection of the divertor detachment radiation front using multi-spectral imaging *Nucl. Fusion* **60** 066017
[31] Perek A. *et al* 2019 MANTIS: a real-time quantitative multispectral imaging system for fusion plasmas *Rev. Sci. Instrum.* **90** 123514
[32] Bates S.C. and Burrell K.H. 1984 Fast gas injection system for plasma physics experiments *Rev. Sci. Instrum.* **55** 934–9
[33] van Berkel M. *et al* 2020 Correcting for non-periodic behaviour in perturbative experiments: application to heat pulse propagation and modulated gas-puff experiments *Plasma Phys. Control. Fusion* **62** 094001
[34] van Berkel M. 2015 Estimation of heat transport coefficients in fusion plasmas *PhD Thesis* Eindhoven University of Technology (https://research.tue.nl/en/publications/estimation-of-heat-transport-coefficients-in-fusion-plasmas)
[35] Wensing M. *et al* 2021 SOLPS-ITER validation with TCV L-mode discharges *Phys. Plasmas* **28** 082508
[36] Ravensbergen T., de Vries P.C., Felici F., Blanken T.C., Nouailletas R. and Zabeo L. 2018 Density control in ITER: an iterative learning control and robust control approach *Nucl. Fusion* **58** 016048
[37] Perek A. *et al* 2021 A spectroscopic inference of flux-resolved edge plasma parameters in detachment experiments on TCV *Nucl. Fusion* (submitted)
[38] Pintelon R. *et al* 2005 Diffusion systems: stability, modeling, and identification (Ottawa, Canada 17 – 19 May, 2005) *Conf. Rec.—IEEE Instrumentation and Measurement Technology Conf.* vol 2 pp 894–9 (https://ewh.ieee.org/soc/im/imtc/imtcup/index.html)
[39] Söderström T. and Bhikkaji B. 2000 Reduced order models for diffusion systems via collocation methods *IFAC Proc.* **33** 977–82

[40] Curtain R. and Morris K. 2009 Transfer functions of distributed parameter systems: a tutorial *Automatica* **45** 1101–16
[41] Janky F., Fable E., Englberger M. and Treutterer W. 2021 Validation of the Fenix ASDEX Upgrade flight simulator *Fusion Eng. Des.* **163** 112126
[42] Van Berkel M. *et al* 2017 New evidence and impact of electron transport non-linearities based on new perturbative intermodulation analysis *Nucl. Fusion* **57** 126036
[43] Curtain R. and Zwart H. 1995 An introduction to infinite-dimensional linear systems theory *Texts Appl. Math.* **21** 698